Variational Assimilation of Slant-Path Wet Delay Measurements from a Hypothetical Ground-Based GPS Network. Part I: Comparison with Precipitable Water Assimilation

SO-YOUNG HA

National Center for Atmospheric Research, Boulder, Colorado, and School of Earth and Environmental Sciences, Seoul National University, Seoul, South Korea

YING-HWA KUO AND YONG-RUN GUO

National Center for Atmospheric Research, Boulder, Colorado

GYU-HO LIM

School of Earth and Environmental Sciences, Seoul National University, Seoul, South Korea

(Manuscript received 20 September 2002, in final form 28 March 2003)

ABSTRACT

With the recent advance in Global Positioning System (GPS) atmospheric sensing technology, slant wet delay along each ray path can be measured with a few millimeters accuracy. In this study, the impact of slant wet delay is assessed on the short-range prediction of a squall line. Since the current GPS observation network in the central United States is not of high enough density to capture the mesoscale variation of moisture in time and space, a set of observing system simulation experiments is performed to assimilate slant wet delay data from a hypothetical network of ground-based GPS receivers using the four-dimensional variational data assimilation technique. In the assimilation of slant wet delay data, significant changes in moisture, temperature, and wind fields within the boundary layer were found. These changes lead to a stronger surface cold front and stronger convective instability ahead of the front. Consequently, the assimilation of slant wet delay produces a considerably improved 6-h forecast of a squall line in terms of rainfall prediction and mesoscale frontal structure.

Previous studies have shown that the assimilation of GPS-derived precipitable water data can improve moisture analysis and rainfall prediction. In order to assess the additional value of slant wet delay data assimilation, a parallel experiment is performed in which precipitable water data is assimilated. The assimilation of slant wet delay data is demonstrated to be superior in recovering water vapor information between receiver sites and in short-range precipitation forecast both in terms of rainfall distribution and intensity. As revealed by atmospheric soundings in the vicinity of the squall line, the assimilation of slant wet delay data more accurately retrieves the temperature and moisture structure in the convectively unstable region.

1. Introduction

With the recent advance in Global Positioning System (GPS) atmospheric remote sensing, ground-based GPS receivers have become an important instrument that can potentially provide high-resolution water vapor measurements at low cost. A receiver on the ground measures delayed GPS radio signals as they propagate through the earth's atmosphere. After eliminating the ionospheric delay with dual frequencies and subtracting the hydrostatic delay from the total tropospheric delay, we can obtain the residual signal, which is referred to as slant wet delay (SWD), and convert it to water vapor quantities using a conversion parameter (Bevis et al. 1994). As each receiver can simultaneously track up to 10 GPS satellites (and the typical observation time interval is 30 s), the collection of all available SWD data can provide information on the small-scale spatial distribution of water vapor around the receiver site. However, since the individual delay signal can be largely affected by noise due to instability of the receiver oscillator, site multipath, etc., an accurate SWD along each ray path has been difficult to obtain. Alternatively, all SWD measurements are projected onto zenith and averaged over a certain time period (e.g., 30 min). The resulting quantity, zenith wet delay (ZWD), provides a good estimate of precipitable water (PW), which represents the integrated water vapor in the vertical column overlying the receiver. The derivation of ZWD and PW can greatly reduce the uncertainties associated with each

Corresponding author address: So-Young Ha, NCAR, P.O. Box 3000, Boulder, CO 80307-3000.
E-mail: syha@ucar.edu

© 2003 American Meteorological Society

SWD measurement by averaging over many epochs and satellites, but it also loses valuable information on the three-dimensional moisture structure around the receiver site. Moreover, the assumption of azimuthal homogeneity limits the accuracy and spatial resolution of GPS-sensed water vapor (Davis et al. 1993; Elosegui et al. 1998).

Recent advances in GPS sensing technology allow the retrieval of SWD with an accuracy of a few millimeters (Ware et al. 1997; Braun et al. 2001). This has encouraged researchers to compare GPS SWD measurements with numerical simulations and to further improve the accuracy of GPS data processing (Vandenberghe and Guo 2000; Pany et al. 2001; Pany 2002; Ha et al. 2002). Now, with the improved accuracy, it would be desirable to directly assimilate GPS SWD measurements (instead of PW) into numerical weather prediction models. As the GPS-sensed slant-path measurement represents an integrated quantity of water vapor along each ray path, it does not provide information on the vertical distribution of water vapor. By assimilating the SWD measurements into a numerical model, three-dimensional moisture structure may be recovered with the help of model dynamics and physics.

Encouraged by the potential of GPS water vapor sensing, there have been several precedent studies on the assimilation of ground-based GPS measurements into weather prediction models and their potential impact on the short-range weather prediction (Kuo et al. 1993, 1996; Guo et al. 2000; MacDonald et al. 2002; De Pondeca and Zou 2001a,b). These studies vary in terms of assimilation variables (precipitable water, zenith total delay, and slant water vapor) and assimilation approaches (nudging, three-dimensional and four-dimensional variational assimilation). In general, the results are positive, and their impact varies depending on the size of the network and the assimilation approaches. However, a direct assimilation of slant wet delay data with a full-physics mesoscale four-dimensional variational data assimilation has not yet been attempted.

At present, a near real-time analysis of GPS precipitable water observations is available from the National Oceanic and Atmospheric Administration/Forecast Systems Laboratory (NOAA/FSL) network and the SuomiNet (Ware et al. 2000), which consists of approximately 125 sites over the United States. However, this network does not have high enough spatial resolution to properly resolve the mesoscale variations of the atmospheric moisture. And slant GPS data are currently available with several day latency from more than 20 sites (www.suominet.ucar.edu), with plans to move toward real time and add more than 100 additional sites (R. Ware 2002, personal communication).

In this study, we design a hypothetical high-density ground-based GPS network in a squall-line area to assess the potential impacts of SWD assimilation on short-range prediction of a prefrontal squall line through a set of observing system simulation experiments (OSSEs; Arnold et al. 1986). Specifically, we assimilate SWD measurements from the network of 64 GPS receivers located in the Oklahoma–Kansas panhandle in the fifth-generation Pennsylvania State University–National Center for Atmospheric Research (PSU–NCAR) Mesoscale Model (MM5) four-dimensional variational (4DVAR) data assimilation system.

The main purposes of this study are: 1) to develop a technique to effectively assimilate GPS SWD measurements into the mesoscale forecast model, 2) to assess the impact of SWD assimilation on the short-range forecast of a prefrontal squall line, and 3) to compare the performance of SWD assimilation with GPS PW assimilation in terms of rainfall prediction and the recovery of moisture structure.

In section 2, the methodology for this study including how to assimilate SWD into the numerical model is described. In section 3, the overview of the selected case and the experiment design are discussed. Section 4 presents the analysis of the OSSE results and section 5 provides a summary and a suggestion for future work.

2. Methodology

a. Variational assimilation

The objective of the variational assimilation is to obtain an optimal solution based on all available observations, background analysis, observation error statistics, background error statistics, and a full-physics forecast model within a certain period of time. The 4DVAR system allows observations to be assimilated in their raw form at any given point in time and space and the model solution is required to fit the observations in a least squares sense. The discrepancy is measured by a cost function J, and the two terms (J^B and J^0) in the cost function are weighted by the inverse of the background error covariance and the observational error covariance, respectively (Zou et al. 1997):

$$\begin{aligned} J &= J^B + J^o \\ &= \frac{1}{2}(\mathbf{x}_0 - \mathbf{x}_b)^{\mathrm{T}}\mathbf{B}^{-1}(\mathbf{x}_0 - \mathbf{x}_b) \\ &\quad + \frac{1}{2}\sum_{r=0}^{n}[H(\mathbf{x}_r) - \mathbf{y}_r]^{\mathrm{T}}\mathbf{O}^{-1}[H(\mathbf{x}_r) - \mathbf{y}_r], \end{aligned} \quad (2.1)$$

where $\mathbf{x}_0$ is the analysis vector consisting of eight model control variables [winds (u, v), temperature (T), specific humidity (q), pressure perturbation (p'), vertical velocity (w), cloud water (q_c), and rainwater (q_r)] at the model initial time $t = t_0$. The corresponding forecast background vector is $\mathbf{x}_b$, and $\mathbf{B}$ the background error covariance matrix. In the present study, $\mathbf{B}$ is diagonal and derived based on Navon et al. (1992). The weightings are calculated as the inverse square of the maximum differences between two forecasts that are 6 h apart. To assimilate the observed data into the 4DVAR system, J^0 and the corresponding forward observation operator

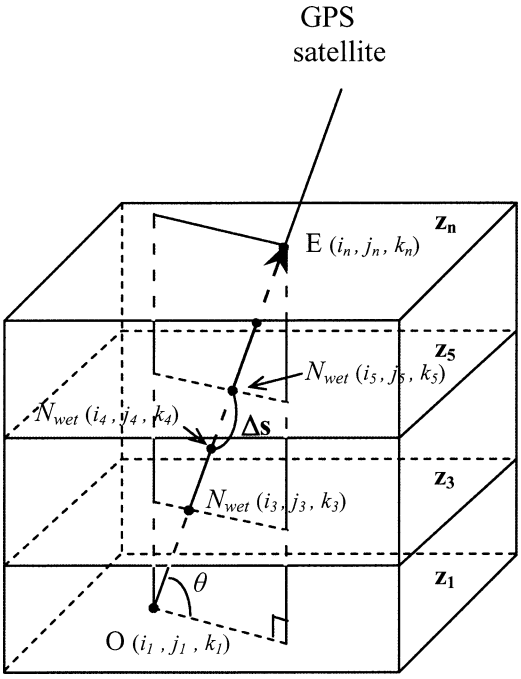

FIG. 1. A schematic of ray integration from a given receiver site (O) to the end point (E) in the model domain; i, j, k indicate three-dimensional grid indices and z_n indicates the reference height at $k = n$, which is simplified by ignoring its horizontal variation; θ is the elevation angle and N_{wet} wet refractivity.

should be developed by users in advance. The observation operator H transforms the model variables $\mathbf{x}_r$ to the observed variables $\mathbf{y}_r$ at time $t = t_r$. Here, the superscript ''T'' stands for transpose; and n is the number of observed time periods. In this study, an error covariance matrix $\mathbf{O}$ is defined as a diagonal matrix with invariant elements, which is the inverse of the measurement error variances, under the assumption that measurements at different sites are uncorrelated. Also, we assume a perfect model framework in (2.1).

In the present OSSE study, to understand the impact of GPS water vapor information on short-term prediction of a squall line, we assimilate water vapor measurements—GPS precipitable water or slant wet delay—without any other conventional observations. Therefore, J^0 will be J^{pw} or J^{swd} in this paper.

b. 4DVAR assimilation of slant wet delay

1) GPS SLANT WET DELAY RETRIEVAL

Microwave radio signals transmitted from GPS satellites to a ground-based receiver are refracted and delayed by the atmospheric gases as they pass through the atmosphere. The delay due to the ionosphere is caused by the charged field of free electrons and can be corrected to millimeter accuracy with the use of a linear combination of measurements at the two GPS frequencies (L1 and L2). In the troposphere, signal delays in transmissions are caused by a variable index of refraction along the ray path. The delay due to the neutral troposphere consists of two components: ''hydrostatic delay'' and ''wet delay.'' Wet delay is caused by tropospheric water vapor along the ray path, and hydrostatic delay by all other atmospheric constituents (Rocken et al. 1995). To a good approximation, refractivity in the troposphere is related to atmospheric pressure [P (hPa)], temperature [T (K)], and water vapor pressure [e (hPa)] at microwave wavelengths as in (2.2) (Boudouris 1963):

$$\text{refractivity } N = (n - 1) \times 10^6 = N_{\text{hydrostatic}} + N_{\text{wet}} = k_1 \frac{P}{T} + k_2 \frac{e}{T^2}, \tag{2.2}$$

where k_1 and k_2 are experimentally determined constants and n is the refractive index. Even though hydrostatic refractivity ($N_{\text{hydrostatic}}$), the first term on the right-hand side of (2.2), contains water vapor effects through pressure, hydrostatic delay is generally called *dry* delay to differentiate itself from the *wet* delay (N_{wet}), which includes the effects of water vapor only. This expression is considered accurate to about 0.5% under normal atmospheric conditions (Resch 1984).

To simulate slant wet delay along each ray path, we integrate wet refractivity [as defined in (2.2)] from a ground-based receiver to a satellite in view as in(2.3):

$$\text{SWD}_i^m = 10^{-6} \int_{\text{receiver}}^{\text{satellite}} N_{\text{wet}}\, ds, \tag{2.3}$$

where m is satellite number, i receiver number, and ds has unit of length (m) along the GPS ray path. Slant wet delay can be linearly related to slant water vapor (SWV) using a conversion parameter Π.

$$\text{SWV} = (\Pi)(\text{SWD}), \tag{2.4}$$

where $\Pi = f(T_m)$ and T_m is a weighted mean temperature of the atmosphere (Davis et al. 1985). Bevis et al. (1994) showed that T_m is strongly related to the surface temperature ($T_m = 70.2 + 0.72\, T_s$) and the conversion parameter Π is approximately 0.15, which implies that 1 mm of integrated water vapor corresponds to a delay of about 6.5 mm. However, the actual value of Π can vary by as much as 20% due to T_m. To avoid errors caused by the assumption regarding T_m, we directly assimilate slant wet delay (instead of slant water vapor) in the present study.

2) RAY INTEGRATION

In this study, we assimilate SWD data with ray paths above 5° elevation angle only. Based on the radar slant range–height diagram (Fig. 3.2 in Rinehart 1989), the bending effect is negligible for rays with an elevation angle greater than 5°. We evaluated the accuracy of straight-line approximation in the estimate of SWD as

compared with a ray-tracing method, and found the approximation to be accurate above 5° elevation angles with less than 1% rms error (Ha et al. 2002). Therefore, we assume that the ray path is a straight line in the ray integration in the 4DVAR system. Zou et al. (1999) used a ray-tracing method, which controls the direction vector of the ray path by calculating the three-dimensional refractivity gradient at each step of the ray integration. The ray-tracing technique has the advantage of accounting for the bending effect of each ray path. But a major shortcoming of this method is the high computational cost, which is about 20 times larger than that of the straight ray-path integration in the present case. In the ray-tracing method, the time-consuming process of ray-path estimation must be included in the minimization procedure, while it only needs to be done once outside the minimization procedure in the straight ray-path integration, for a given elevation and azimuth angle. Thus, the latter is very efficient and very attractive for the 4DVAR system.

A schematic of ray integration is shown in Fig. 1. Wet refractivity (N_{wet}) is first computed from all gridded pressure, temperature, and specific humidity fields at every half-sigma level and is then horizontally interpolated to the point at which the ray path intercepts each level by a 16-point biparabolic interpolation (Guo and Chen 1994). In order to increase computational accuracy, each sigma level is subdivided into two levels and wet refractivity at the intermediate level is estimated by log-linear vertical interpolation. To calculate slant wet delay along the ray path, wet refractivity is integrated from the ground receiver site $[O(i_1, j_1, k_1)]$ to the model top $[E(i_n, j_n, k_n)]$. Once we find the start point O and the end point E in the three-dimensional model grid domain, we can integrate the ray path:

$$\text{SWD} = 10^{-6} \sum_{m=2}^{n} \frac{[N_{\text{wet}}(i_{m-1}, j_{m-1}, k_{m-1}) + N_{\text{wet}}(i_m, j_m, k_m)]}{2}(\Delta s)$$

$$\Delta s = \sqrt{[(i_m - i_{m-1})^2 + (j_m - j_{m-1})^2] \times \text{dis}^2 + (z_m - z_{m-1})^2}, \tag{2.5}$$

where the subscript m is the vertical-level index, z the reference height (m), and dis the horizontal grid distance of the forecast model (m). Equation (2.5) and the second term (N_{wet}) in (2.2) correspond to the observation operator H for SWD in (2.1). For simplicity, we ignore the horizontal variation of the reference height field and use the one-point values above the receiver site (i_1, j_1). In the present OSSE study, the hypothetical observation network is located over the southern Great Plains in the United States, which has a relatively flat topography except near the western lateral boundaries (Fig. 2b). Therefore, terrain height at each observation site in the assimilation is fairly close to the ''true'' topography, which is obtained from the 3-km nature run (which will be explained in section 3). Differences in terrain heights between the 27-km assimilation model and the simulated observation are less than 100 m at all sites, and the effect of terrain differences on slant wet delay is less than 1% on average in this case. The errors in the slant wet delay observation operator introduced by the approximation of a straight ray path and the use of smooth model terrain height are neglected in the present OSSE study, and thus not included in the error covariance matrix in the slant wet delay assimilation.

Slant wet delay observations are first simulated from the nature run through the method described above as instantaneous values valid at every 5 min. To more realistically simulate GPS measurements, we generate random errors that are of uniform distribution with a random number generator and then add these errors to the ''perfect'' slant wet delay observations. The magnitude of random errors is similar to that of the real measurement errors as stated in the next section.

3) Slant wet delay measurement errors

In the actual observations, the measurement error of slant wet delay is estimated by comparing GPS slant wet delay measurements with those from radiometers pointing to the same direction (at the same azimuth and elevation angles). The slant wet delay in the raw GPS signal is obtained after accurately modeling and accounting for the clock errors, geometric delays, hydrostatic delay, and ionospheric delay. All slant path signals are then projected onto zenith and averaged over a certain period of time under the assumption that the atmosphere is azimuthally homogeneous (Niell 1996); this is called the zenith wet delay. By validating the ZWDs against other independent measurements (e.g., from a radiometer), we can estimate the observation error of ZWD. The error of ZWD is then projected back to the elevation angle of an individual ray path (assuming an isotropic atmosphere around the receiver site). This is called an isotropic error, which is dominated by the systematic error between a ground-based GPS receiver and a water vapor radiometer. Braun et al. (2001) estimated the nonisotropic errors of GPS slant water vapor measurements from the NOAA/FSL network and showed the statistics for bins of 5° elevation angles (see Table 1 in their paper). When we assume that the isotropic and the nonisotropic error are not correlated with

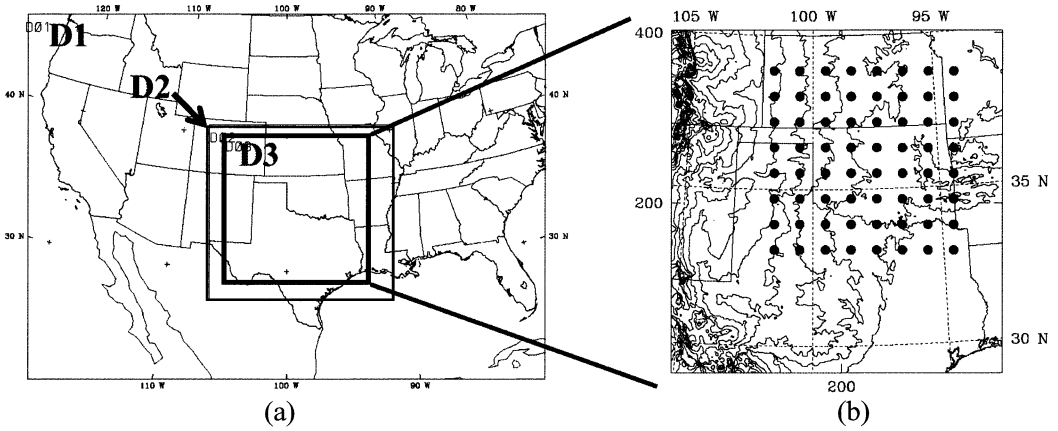

FIG. 2. (a) Domains of observing system simulation experiments. Domain 3 (D3) is used for both the nature run (at 3-km resolution) and 4DVAR experiments (at 27-km resolution). Domain 2 (9-km resolution) is used to provide lateral boundary condition for domain 3 in a one-way nested mode. (b) Terrain height simulated in the 3-km nature run and 64 hypothetical GPS observation network with 90-km spacing. Contour interval is 200 m.

each other, total slant wet delay measurement error (SWD_{err}) can be expressed as in (2.6).

$$SWD_{err} = \sqrt{(\text{Isotropic\_err})^2 + (\text{Nonisotropic\_err})^2} \tag{2.6}$$

In this OSSE study, we assume that the ''simulated'' slant wet delay has errors with magnitudes similar to those of the total real measurement errors (shown by the solid line in Fig. 8b). The magnitude of the nonisotropic error is approximately half of the isotropic component at 10° elevation angle in this study.

c. 4DVAR assimilation of precipitable water

In the previous studies (Kuo et al. 1993, 1996; Guo et al. 2000), precipitable water was calculated using (2.7) under the assumption of hydrostatic balance.

$$PW = \frac{p^*}{g} \sum_{K=1}^{KX} q(K)\Delta\sigma(K), \tag{2.7}$$

where $q(K)$ is the analysis of specific humidity at the Kth layer, $\Delta\sigma(K)$ is the thickness of the Kth layer, and KX is the total number of layers. Here, $p^* = p_0 - p_s$, where p_s is the surface pressure, p_t is the pressure at the top of the model (100 hPa), and g is the acceleration due to gravity.

In the actual GPS sensing, however, precipitable water is derived from zenith wet delay:

$$PW = (ZWD)(\Pi) \tag{2.8}$$

The value Π is the same as that in (2.4). The zenith wet delay is an estimate, commonly based on the principles of least square estimation, which utilizes the zenith-mapped slant wet delays from a specified time window and sampling interval. In the 4DVAR system, the assimilation of ZWD was implemented under the assumption that an average of all slant wet delays would accurately represent this estimation. The average is represented through the following equation:

$$ZWD = \frac{1}{(nt \times nr)} \sum_{t=1}^{nt} \sum_{j=1}^{nr} SWD_j^t \sin\theta_j^t, \tag{2.9}$$

where nr is the total number of satellites in view at a given time at each station, and nt is the observation frequency. As we assume that slant wet delay measurements are available every 5 min and precipitable water is estimated at 30-min intervals, nt is 6 in this study.

For convenience, we refer to PW in (2.7) as PW_q, and PW in (2.8) as PW_{swd}. If the water vapor is homogeneously distributed and the rays scan the atmosphere uniformly in space during the observation period, the error due to the different definition of precipitable water can be neglected to a good approximation. However, due to the inhomogeneity in sampling the data from GPS receivers and the temporal and spatial variation of the atmospheric water vapor, the PW_{swd} can be quite different from PW_q in (2.7), especially when a squall line is approaching. An estimate of the rms differences between PW_q and PW_{swd} is 2.9 mm based on the results of the nature run, which is about twice as large as the GPS PW measurement error of 1.5 mm. Therefore, such error cannot be ignored and one should not treat PW_{swd} as PW_q. Thus, we simulate precipitable water following the same algorithm (2.8) and (2.9) as that used in the real GPS measurement. [In turn, (2.8) and (2.9) correspond to the observation operator for PW in (2.1).] We first calculate slant wet delay along each ray path, scale it to the zenith, and then average all the zenith-mapped slant wet delays for a 30-min time period to calculate PW_{swd}.

3. Experiment design and case description

a. Experiment design

We first perform the ''nature'' run with a 3-km grid mesh and 50 vertical layers using the MM5 (Grell et al.

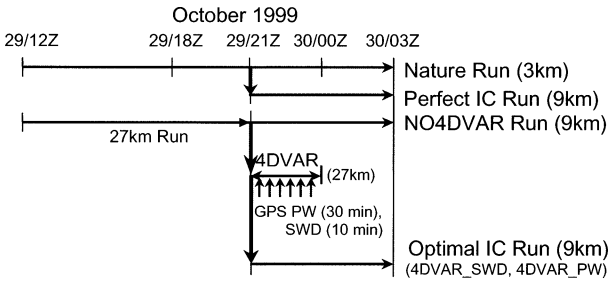

FIG. 3. Schematic diagram of OSSEs design.

1994). This run is initialized at 1200 UTC 29 October, and is integrated for 18 h. The computational domain (D3 in Fig. 2) contains an array of 403 × 388 grid points. In this run, the Reisner-1 mixed-phase microphysics and the National Centers for Environmental Prediction (NCEP) Medium-Range Forecast (MRF) model planetary boundary layer (PBL) scheme (Hong and Pan 1996) are employed, but no cumulus parameterization is used. The forecast results from the nature run are used to simulate slant wet delay measurements from a hypothetical network of GPS receivers. This is done by integrating wet refractivity along each ray path under the assumption that the ray path is a straight line from a fixed station to each GPS satellite as explained in section 2b. For the satellite positions, the actual orbit data are used. The hypothetical network consists of a total of 64 GPS receiver sites regularly distributed over the Oklahoma–Kansas region with 90-km spacing where the squall line is initiated (Fig. 2b).

The basic set of our OSSE design includes Perfect_IC run, NO4DVAR run, 4DVAR_SWD run, and 4DVAR_PW run. All 4DVAR experiments are performed at 27-km horizontal resolution (a 45 × 43 grid mesh) using the MM5 4DVAR system (Zou et al. 1997). All forecast runs are performed at 9-km horizontal resolution (133 × 127 grid points) with 23 layers in the vertical. Since the vertical resolution is considered to be important in the slant wet delay calculation, we use the same vertical resolution of 23 layers in 4DVAR experiments as in all forecast runs, while we reduce the horizontal resolution from 3 km (in the nature run) to 9 km (in the forecast run) and 27 km (in the 4DVAR model) due to the high computation cost. In our 4DVAR runs, the CPU cost of the 9-km model was about 20 times larger than the 27-km model for 40 iterations. The 23 vertical layers are defined at σ = 0.05, 0.15, 0.25, 0.35, 0.425, 0.475, 0.525, 0.565, 0.595, 0.625, 0.655, 0.685, 0.71, 0.73, 0.75, 0.775, 0.805, 0.835, 0.865, 0.895, 0.925, 0.955, 0.985. In the 27-km MM5 4DVAR system, Grell cumulus parameterization, Bulk PBL, and an explicit moisture scheme are used, while the 9-km forward runs use Kain–Fritsch cumulus scheme, the Reisner-1 mixed-phase microphysics scheme, and the Blackadar PBL scheme.

In order to provide an upper-bound benchmark in terms of forecast accuracy for the data assimilation experiments, we conduct experiment 1—''Perfect_IC'' run. The initial condition for this experiment is obtained by taking the model fields at every third grid point of the nature run at 2100 UTC 29 October. This experiment represents a case in which the best possible initial condition is available for a forecast model at 9-km resolution. The deviation of this run from the nature run is primarily caused by model errors (difference between 3- and 9-km grid, and their associated physical parameterization schemes).

Experiment 2 is a ''no data assimilation (NO4DVAR)'' run. This experiment represents a lower-bound benchmark, reflecting the accuracy of a forecast model initialized by a typical operational analysis. In order to provide an initial condition for this experiment, we first conduct a 27-km MM5 experiment using the NCEP global analysis at 1200 UTC 29 October as the initial condition. The 9-h forecast from this 27-km run is then linearly interpolated to the 9-km grid and used as the initial condition for experiment 2.

Experiment 3, is the ''slant wet delay assimilation (4DVAR_SWD)'' experiment. Through the 4DVAR assimilation of slant wet delay over a 3-h time window from 2100 to 0000 UTC 30 October, the optimal initial condition is obtained at 2100 UTC. Slant wet delay measurements are assimilated at 10-min time intervals. The initial condition of experiment 2 at 2100 UTC 29 October is used as the gridded analysis data for the background term of the cost function in the 4DVAR system.

Experiment 4, is the ''precipitable water assimilation (4DVAR_PW)'' experiment. To investigate the relative impact of SWD to PW_{swd}, we perform the 4DVAR experiment of PW_{swd} [as defined in (2.8)]. The observation time interval of SWD measurements for PW_{swd} estimates is 5 min. For the averaging over a 30-min time period, a temporal projection operator is needed in the cost function for PW_{swd}.

TABLE 1. Summary of observing system simulation experiments design.

	Nature run	Forward run	4DVAR run
Resolution	3 km, 50 levels	9 km, 23 levels	27 km, 23 levels
Microphysics	Reisner-1	Reisner-1	Explicit
PBL	MRF	Blackadar	Bulk
Cumulus parameterization	N/A	KF	Grell
Simulation time (1999)	2100 UTC 29 Oct	2100 UTC 29 Oct	2100 UTC 29 Oct to 0000 UTC 30 Oct

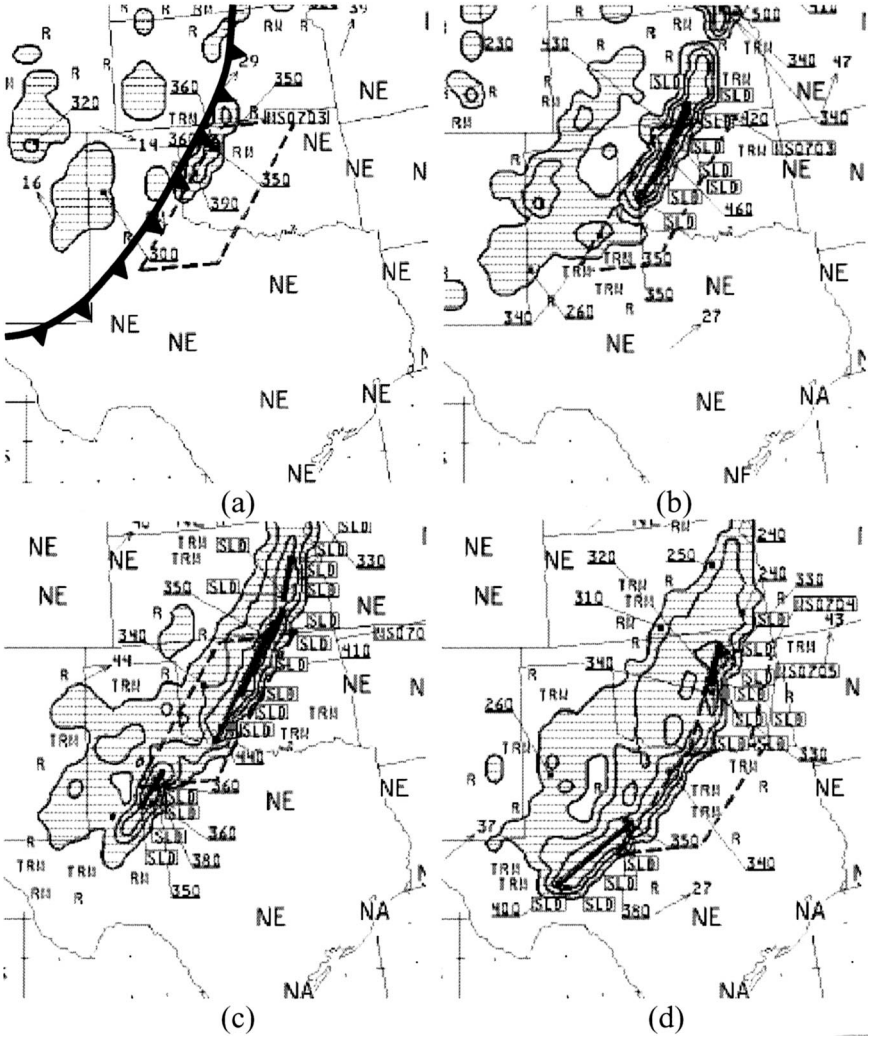

FIG. 4. National Weather Service radar summary for (a) 2135 and (b) 2335 UTC 29 Oct, and (c) 0235 and (d) 0535 UTC 30 Oct 1999. Radar echoes are shaded, and the surface cold front is marked in (a). Dashed boxes are the areas for which the National Severe Storms Forecast Center issued severe weather watches.

All forecast runs are conducted at the 9-km horizontal resolution from the four different sets of initial condition to investigate the impact of slant wet delay on short-term precipitation forecast. By using different physics in the 9-km forward run from the ones in the 3-km nature run, we partially remove the identical-twin problem in this study. Figure 3 and Table 1 provide an illustration and a summary of the experiment design, respectively.

b. Case description

A squall line was initiated over the Kansas–Oklahoma panhandle on 29 October 1999 when a surface cold front moved into a convectively unstable environment. The development of mesoscale convective systems and squall lines in this region is often attributed to the special geography and topography of the region: the Rockies to the west, the high Mexican plateau to the southwest, and the Gulf of Mexico to the southeast. The structures and evolutions of the squall lines over the south-central United States have been studied by many authors (Carlson et al. 1980, 1983; Hobbs et al. 1990; Locatelli et al. 1995, 1998; Martin et al. 1995; Martin 1998).

With the advance of the surface cold front, the line convection formed at 2135 UTC 29 October 1999 over northwestern Oklahoma and developed into a prefrontal squall line producing a maximum 24-hr rainfall amount of 89.8 mm around Lamont, Oklahoma. Figure 4 shows National Weather Service radar summaries over the south-central United States during the squall-line passage. In the 3-km nature run, however, the simulated precipitation (which is modeled by explicit moisture

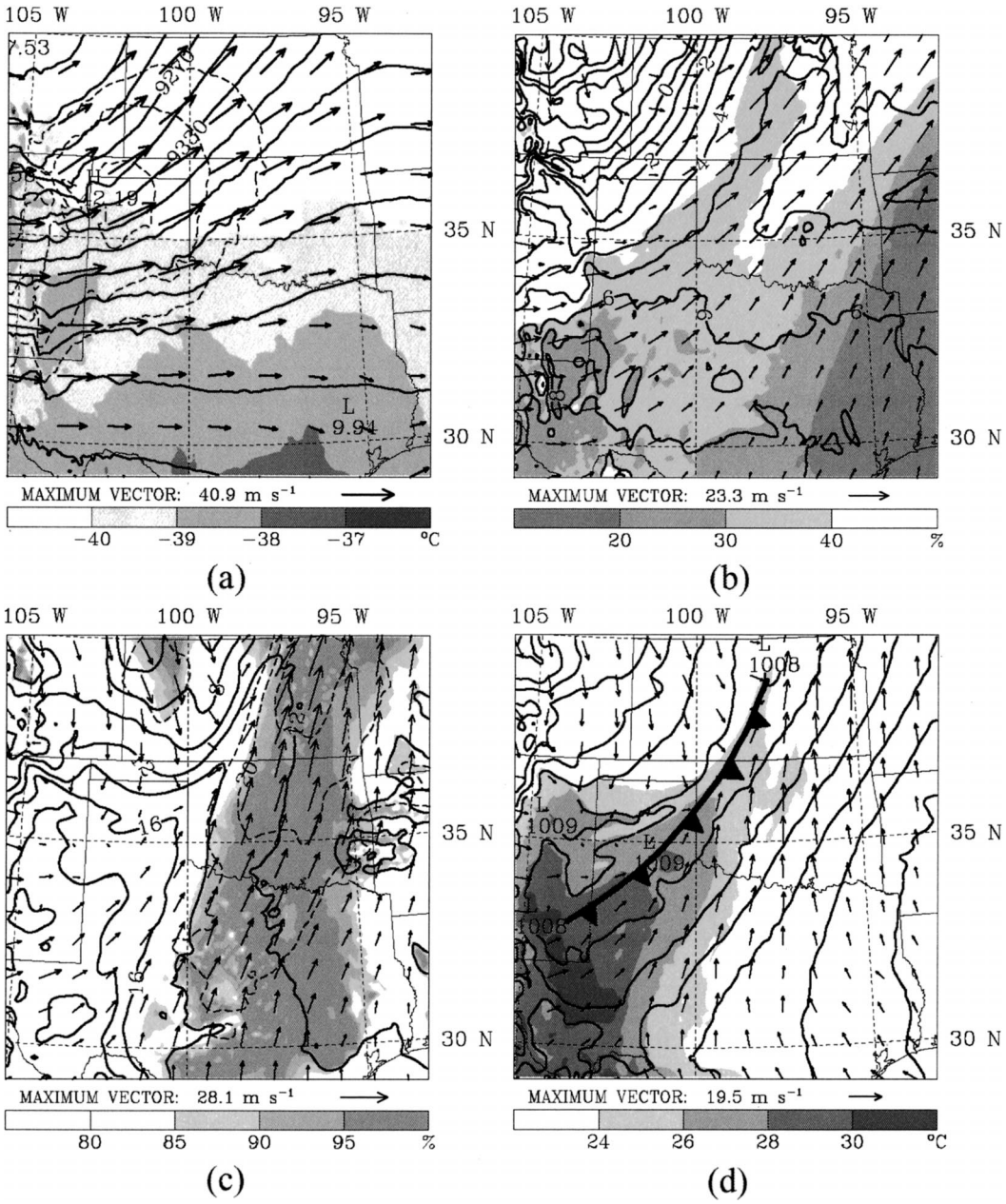

FIG. 5. Simulations from the Perfect_IC run at 2100 UTC 29 Oct 1999. (a) Geopotential height (solid line), horizontal wind speed (dashed line), horizontal wind vectors, and temperature (shaded) at 300 hPa. (b) Temperature (solid line), horizontal wind vectors, and relative humidity (shaded) at 700 hPa. (c) Temperature (solid line), horizontal wind vectors, horizontal wind speed (dashed line), and relative humidity (shaded) at 850 hPa. (d) Sea level pressure (contours), horizontal wind vectors, and temperature (shaded) at the surface. Contour interval is (a) 30 m (solid line) and 5 m s^{-1} (dashed line), (b) 1°C (solid line), (c) 2°C (solid line) and 5 m s^{-1} (dashed line), and (d) 2 hPa, respectively. The dashed line indicates the horizontal wind speed greater than (a) 30 and (c) 15 m s^{-1}. Surface cold front is marked in (d).

scheme) did not occur until 0000 UTC 30 October. Under the OSSE framework, the Perfect_IC run represents the best possible performance of a 9-km model and the goal of the 4DVAR assimilation is to obtain a solution as close as possible to the Perfect_IC. Therefore, we choose to verify the results of our 4DVAR experiments against the Perfect_IC run. It is important to recognize that Perfect_IC run is by no means ''perfect.'' The Perfect_IC run, when verified against the nature run (not shown) or the observed radar echoes (Fig. 4), contains considerable forecast errors in terms of the onset time and the location of the convective rainband. This is

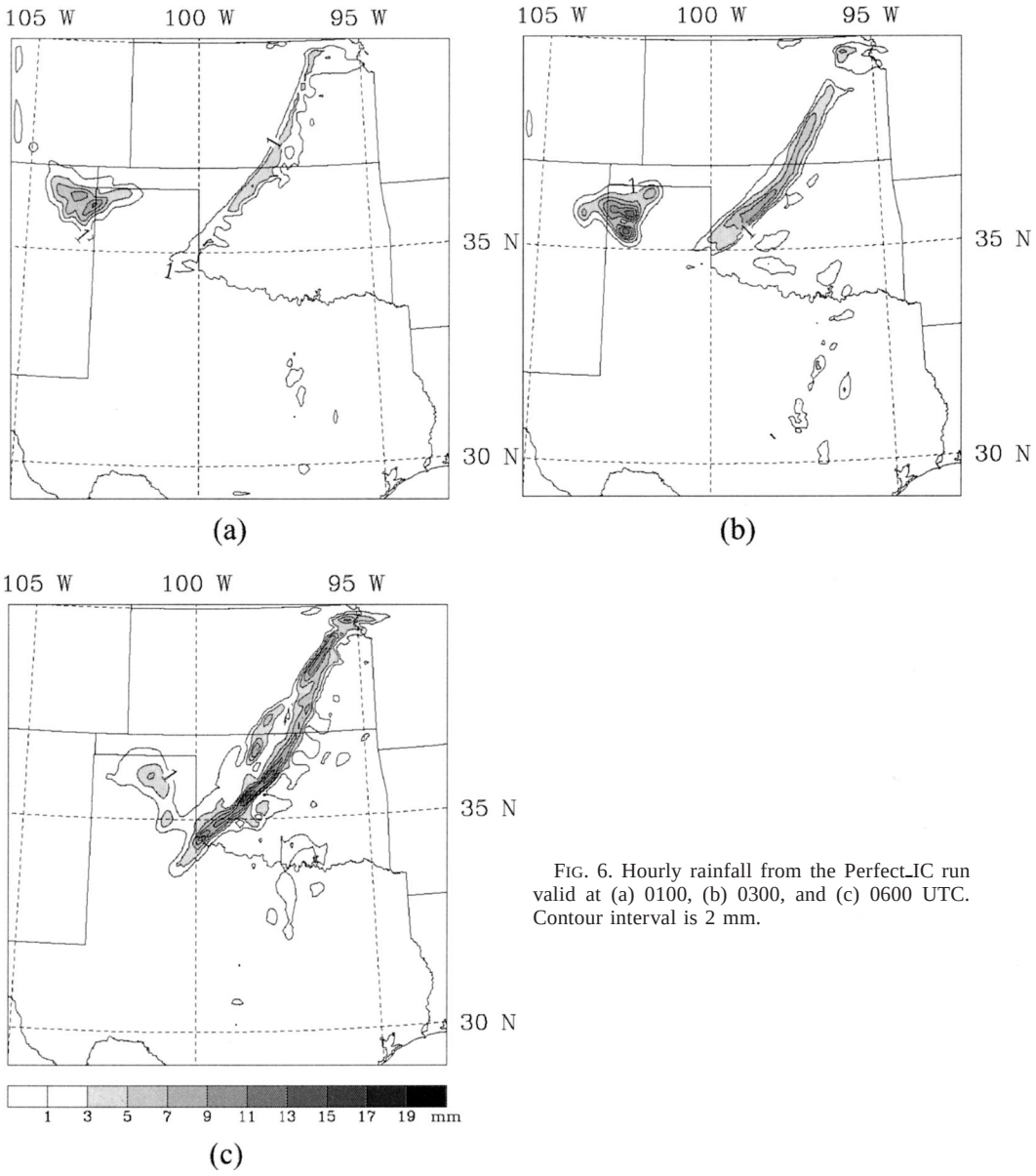

FIG. 6. Hourly rainfall from the Perfect_IC run valid at (a) 0100, (b) 0300, and (c) 0600 UTC. Contour interval is 2 mm.

unavoidable, as the treatment of convection in a 9-km model through cumulus parameterization is quite different from that of a 3-km model with explicit microphysics. The difference between the 9-km Perfect_IC run and the nature run provides a realistic estimate of errors associated with a typical mesoscale forecasting model in its handling of convection.

Here, we describe the synoptic pattern before the formation of the squall line as simulated by the Perfect_IC Run (Fig. 5). At 2100 UTC 29 October 1999, with the approach of an upper-level trough at 300 hPa, a strong upper-level jet is coming off the Rockies and the warm and dry air is advected to central Kansas–northwestern Oklahoma (Fig. 5a). At the surface, a trough is located over the northeastern Kansas–northwestern Texas region, where there is a confluence of the cool, moist air from the Gulf of Mexico and the cold, dry air from Colorado (Fig. 5d). At this time, the cool, moist air is being advected from the south along a strong low-level jet (LLJ) with a maximum wind speed of 28.1 m s^{-1} at 850 hPa. A large shaded area in which relative humidity is greater than 80% is located in the downstream region of the surface cold front (Figs. 5c and 5d). At 700 hPa, a warm and dry tongue along with the southwesterlies from the high Mexican plateau extends to northern Kansas and is superimposed over the low-level moist air to form a convectively unstable region (Fig. 5b). The surface cold front moves southeastward with a speed of 15.5 km h^{-1} and is gradually enhanced. The surface cold

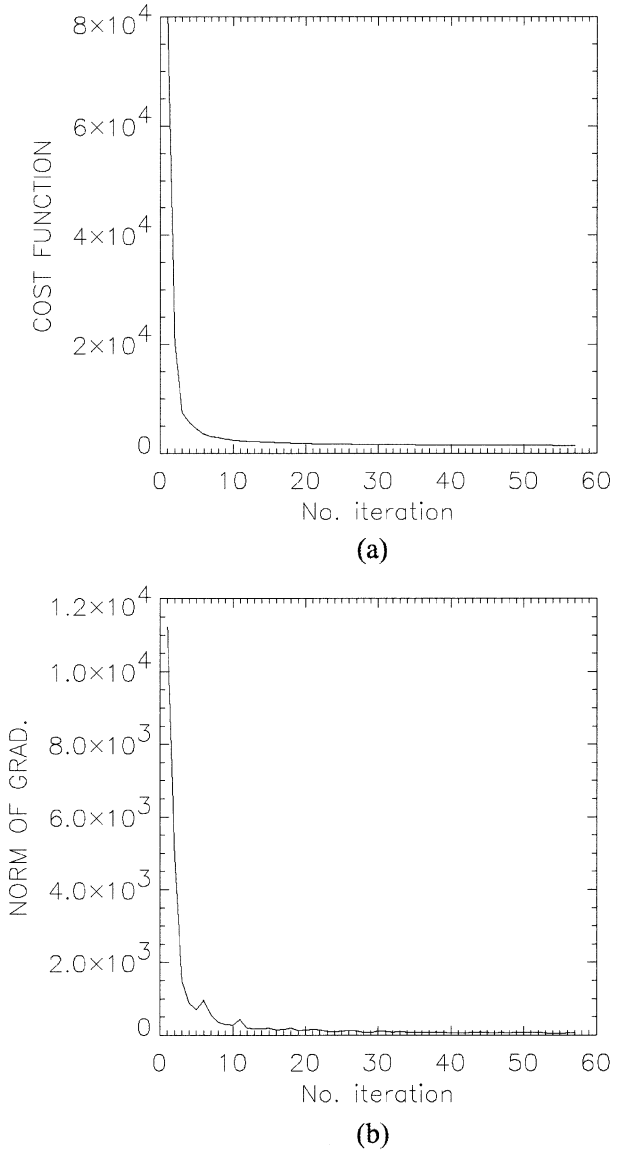

FIG. 7. (a) Cost function J and (b) the norm of gradient with respect to the number of iterations in 4DVAR_SWD.

front acts as a barrier to the low-level moist air flowing toward the front and triggers convection.

After a few rain cells first appear in the vicinity of the Kansas–Oklahoma border at 0000 UTC 30 October (not shown), the convection is quickly organized into a squall line ahead of the surface front at 0100 UTC and continues to intensify while moving southeastward with time (Fig. 6). The maximum hourly rainfall at 0600 UTC 30 October (9-h forecast) is 14.3 mm h^{-1}.

As the main objective of this study is to assess the impact of the slant wet delay measurements from a network of ground-based GPS receivers on the forecast of the squall line, the assimilation time window is set from 2100 UTC 29 to 0000 UTC 30 October, a 3-h time period before the squall line is formed.

4. Results

a. An optimal solution from the 4DVAR assimilation

Figure 7 shows the cost function and the norm of the gradient during the minimization process in the 4DVAR assimilation of slant wet delay (4DVAR_SWD). Both the cost function and the gradient norm decrease very quickly and the minimization process stops at 57 iterations. Since the value of the cost function is reduced by almost 98% and the norm of gradient by about 99% at iteration 40, we take the optimal initial condition at iteration 40 and perform the forward run with it.

To assess the effectiveness of 4DVAR experiments, differences between modeled and observed slant wet delays during the 3-h assimilation window are plotted before and after the minimization process (Fig. 8). Before the minimization process in 4DVAR_SWD, slant wet delays retrieved from the model first guess are much smaller than the ''observed'' values (simulated from the nature run), which implies that the model initial condition is much drier than the ''true'' atmosphere. Large differences (ΔSWD) at the low elevation angle (especially around 10°) are due to the long ray path and do not mean that relative errors of GPS slant wet delay depend on the elevation angle of each ray path. After 40 iterations in the minimization process, rms error is reduced by as much as 90% and the large negative bias of -22.57 mm is almost diminished. It is also notable that the errors are greatly reduced for low elevation angles, which implies the accuracy of capturing the low-level moisture content is greatly improved. These results confirm that the model state in the 4DVAR experiment provides a best fit to the observations through the minimization process.

Even though the 4DVAR system can obtain an optimal solution mathematically, it does not guarantee that the solution is physically meaningful. To examine how the 4DVAR assimilation of slant wet delay changes the atmospheric state in the minimization process, we examine the changes of model control variables with iterations. Figure 9 shows the water vapor mixing ratio at the lowest sigma level ($\sigma = 0.985$) at iteration 0, 5, 20, 40. With increased iterations, the low-level moisture is increased near the border of Kansas–Oklahoma where the squall line forms in a few hours. Comparing the moisture distribution before minimization (Fig. 9a) and after minimization (40 iterations) (Fig. 9d), we note that the contour of 11 g kg^{-1} is expanded to southeastern Kansas. As a result, specific humidity in this area is increased by 1.0 g kg^{-1}. The corresponding analyses for the temperature and horizontal wind fields at the same lowest sigma level are shown in Fig. 10. Note that slant wet delay is a function of three-dimensional pressure, temperature, and water

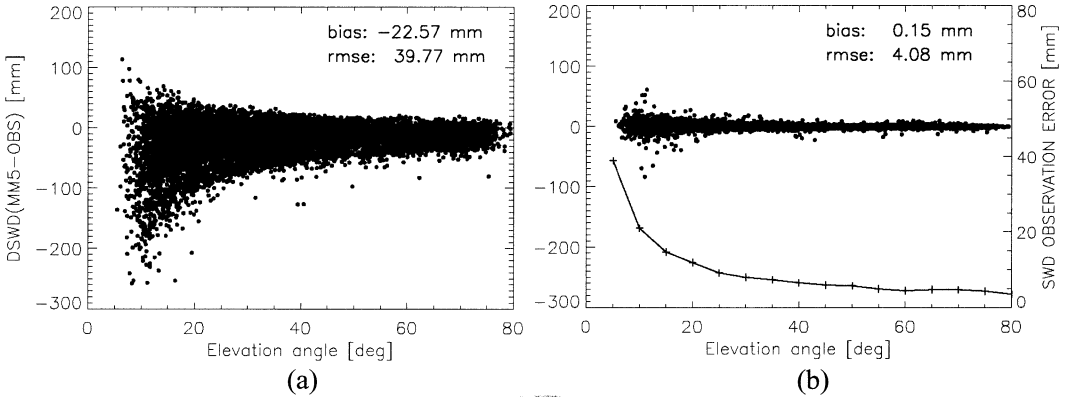

FIG. 8. Differences between modeled and observed slant wet delays during the 3-h assimilation time window (a) before and (b) after 4DVAR experiments (4DVAR_SWD). (b) curve with symbols + indicates the total GPS slant wet delay measurement error for each bin of 5° elevation angles, values for SWD measurement errors are shown at right.

vapor. Through the assimilation of SWD, surface temperature is increased by more than 1°C over the squall line area, and the pressure perturbation field is reduced by as much as 0.1 hPa (thick dashed lines in Fig. 10d). Also, it is interesting to note that though SWD data does not contain information on the wind fields, the horizontal wind fields are enhanced by up to 3.5 m s^{-1} in the surrounding area due to dynamic adjustment. Brooks et al. (1993) showed that the structure of a simulated convective storm changed significantly when the low-level temperature was altered by 1°C. In this case, the changes in temperature and moisture amount near the surface, caused by SWD assimilation, contributed to the on-time initiation of a squall line by enhancing the cross-frontal gradient of the temperature field and the frontal circulation and inducing low-level moisture convergence ahead of the front (which will be shown in Fig. 13a).

Even though slant wet delay is an integrated value along each ray path, it is mostly controlled by the low-level moisture. Therefore, we expect the impact of SWD assimilation to reach the entire boundary layer rather than just being confined to the lowest sigma level. Sensitivity of moist convection to boundary layer thermodynamic parameters has been examined in a few previous studies (Lee et al. 1991; Crook 1996). In particular, Crook (1996) found that convective initiation is most sensitive to surface temperature and moisture perturbations. Moreover, through high-resolution, nonhydrostatic numerical model simulations, he showed that variations in boundary layer temperature and moisture that are within typical observational uncertainties (1°C and 1 g kg^{-1}, respectively) could make the difference between no convection and an intense convective storm. The twice-daily upper-air soundings and the surface measurements are not adequate to provide an accurate initial condition for high-resolution mesoscale models. The assimilation of GPS SWD measurements can potentially address this need. To examine if the assimilation of slant wet delay can improve the atmospheric structure in the boundary layer, we show, in Fig. 11, the differences in water vapor mixing ratio, temperature, and three-dimensional circulation vectors before and after minimization in the vertical cross section along the line AA′ in Fig. 9d. Figure 11 indicates that the assimilation of slant wet delay moistens the entire atmosphere, especially the boundary layer, by as much as 1.5 g kg^{-1} where the squall line will be initiated. The moistened region (the shaded area) is also overlapped by the region of positive temperature changes (solid line). As a result, the cross-frontal temperature and moisture gradients associated with the differential development of the boundary layer aid to strengthen the surface cold front and to initiate the convection at the correct location. The strong rising motion immediately behind the moistened boundary layer, associated with enhanced frontal circulations, induces strong low-level moisture convergence ahead of the surface cold front and triggers the release of the convective instability. As will be shown later, these changes in the initial state significantly improve the model's skill in forecasting the onset time and the location of the squall line.

b. Forecasting the evolution of the squall line

1) COMPARISON WITH NO4DVAR

In section 4a, we showed that the assimilation of slant wet delay produces a favorable condition for convective initiation, especially over the region where the squall line is initiated. It would be interesting to see how the improved initial state (especially in the low-level atmosphere) affects the prediction of the squall line. Bear in mind that the line convection forms 4 h into the forecast.

First, the time evolution of equivalent potential temperature and horizontal wind vectors along the cross section perpendicular to the squall line is shown in Fig. 12. The left panels are 4DVAR_SWD and the right panels are NO4DVAR at (Figs. 12a,b) 0 and (Figs. 12c,d) 3 forecast hours. The location of the cross section is the

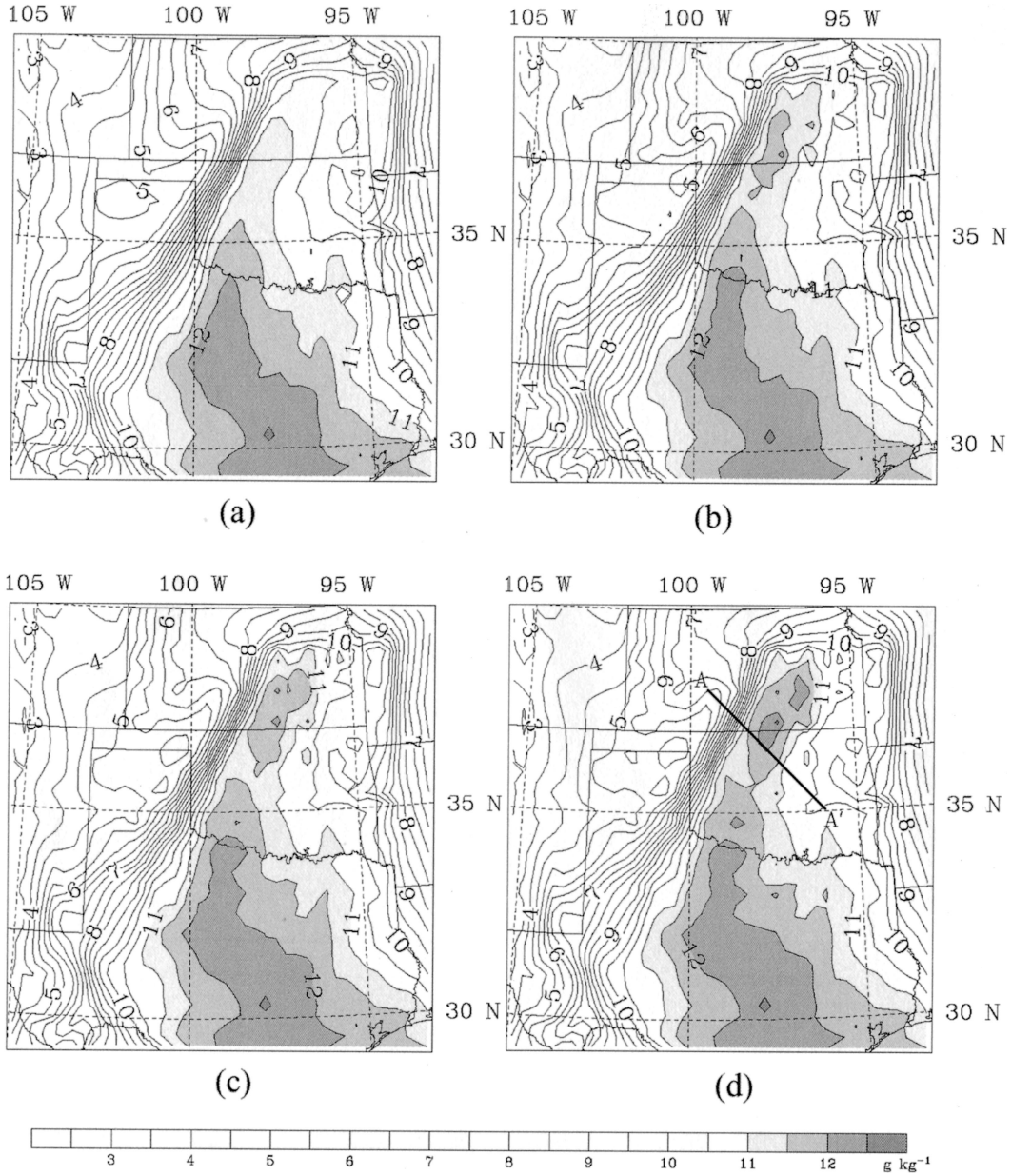

FIG. 9. Water vapor mixing ratio at the lowest sigma level ($\sigma = 0.985$) at the initial time valid at 2100 UTC 29 Oct during the minimization process at iteration (a) 0, (b) 5, (c) 20, and (d) 40. The area greater than 11 g kg^{-1} is shaded. Contour interval is 0.5 g kg^{-1}.

same as that of Fig. 11. The distribution of equivalent potential temperature shows two distinct air masses: the strong southerly moist air in the lower level (the shaded area) and the dry southwesterlies above the moist air around 2-km height. (For a clear identification, we use the contour of 316 K as an indicator of the dry air mass in Fig. 12, and mark it as a thick dashed line). The southwesterly dry air is advected from the arid Mexican plateau and forms a lid over the moist airstream at the initial time (Fig. 12a,b). Comparing with the results of NO4DVAR, the air mass below 2 km is much moister and the dry tongue over the moist air (the thick dashed line) is drier in 4DVAR_SWD, which means that the moisture gradient in 4DVAR_SWD is stronger than in NO4DVAR at the model initial time of 2100 UTC 29 October. The location of the surface cold front (▲), as estimated by the discontinuity of temperature gradient at the surface, is at the 80-km distance mark in 4DVAR_SWD, which is about 10 km ahead of that in NO4DVAR. By 0000 UTC 30 October, a narrow plume of high θ_e has reached about 3-km altitude and the zone of strong gradient of θ_e at the surface has moved about

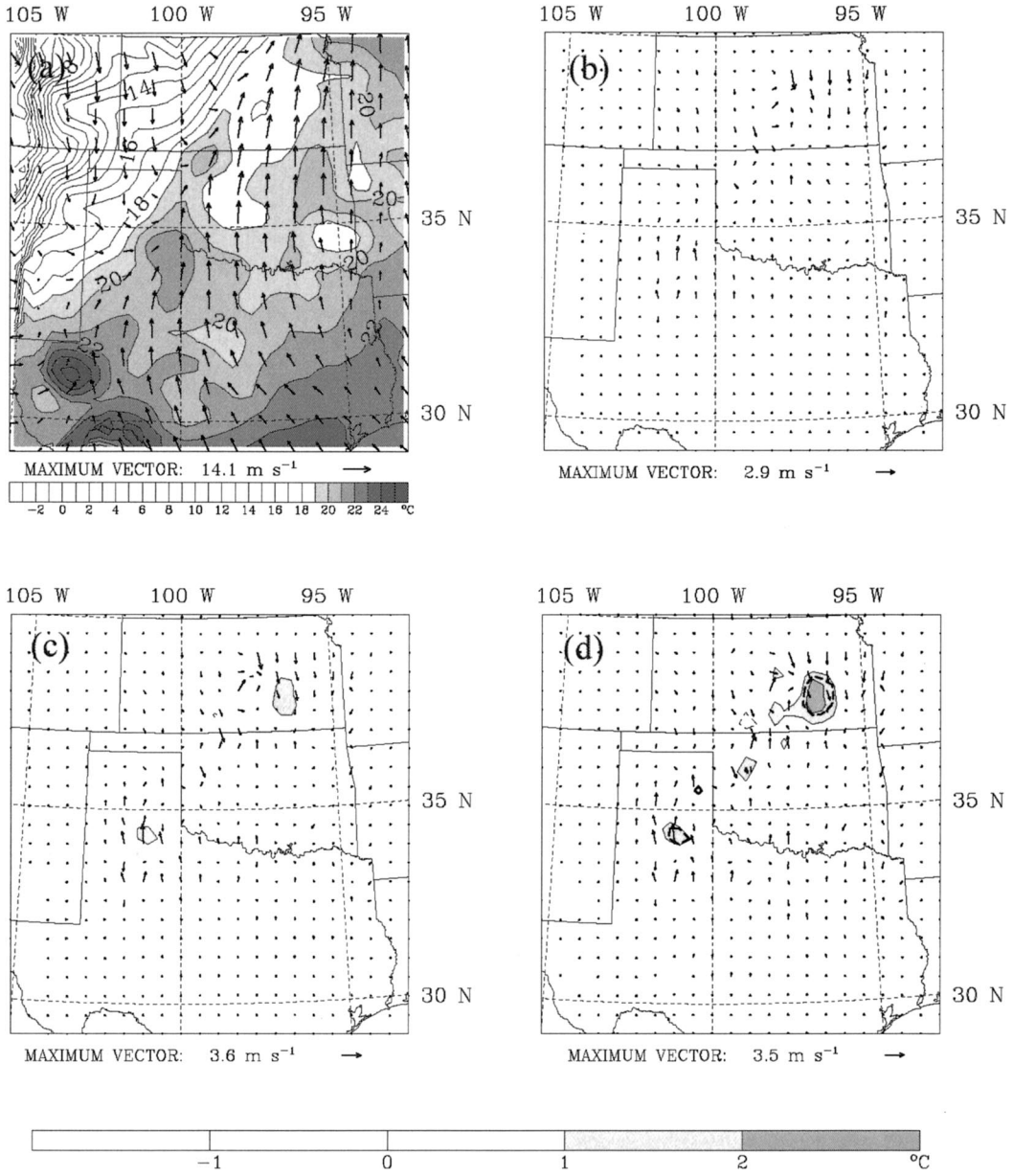

FIG. 10. Temperature and horizontal wind vectors at the lowest sigma level ($\sigma = 0.985$) (a) at the initial time valid at 2100 UTC 29 Oct and their changes during the minimization process after iteration (b) 5, (c) 20, and (d) 40. The shaded area is greater than (a) 18°, and (b), (c), (d) 1°C. Contour interval is 1°C and the negative value is indicated as a dashed line. (d) The thick dashed line indicates negative pressure perturbation differences between after and before minimization with contour interval of 0.1 hPa.

20 km farther downstream in 4DVAR_SWD (Fig. 12c). Meanwhile, a strong lid over the moist air still exists in NO4DVAR at this time (Fig. 12d). The surface cold front is located at the 160-km distance mark in 4DVAR_SWD, which is 60 km farther downstream (to the southeast) than in NO4DVAR. By 0100 UTC 30 October, finally, moist air in NO4DVAR begins to break through the lid to develop convection, while the squall line has already formed in 4DVAR_SWD (not shown).

Watson and Blanchard (1984) and Fankhauser (1988) have shown that the surface moisture convergence field is a useful predictor for storm initiation through observational studies. But Crook (1996) indicated that significant surface moisture convergence could not guarantee the initiation of moist convection because the unstable air at the surface cannot be lifted to the LFC if the negative area of a sounding [convective inhibition (CIN)] is sufficiently large. Thus, he suggested that the integrated moisture convergence through the depth of the boundary layer would be more useful for predicting convective

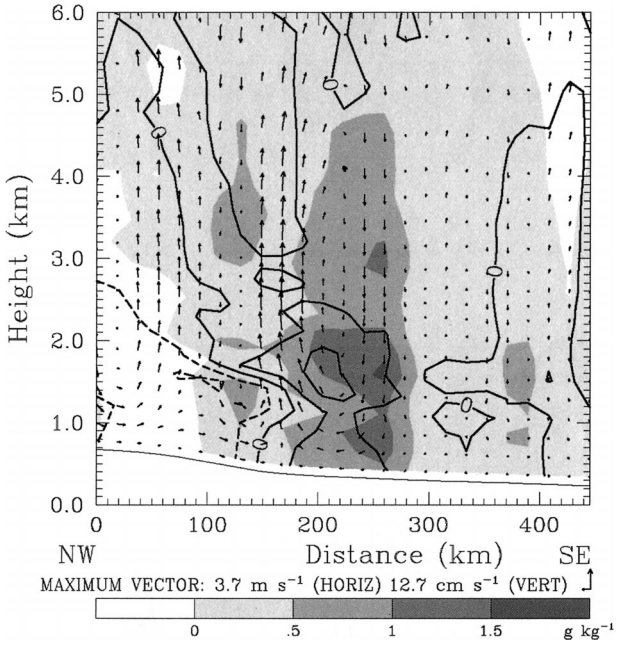

FIG. 11. Differences between ''before'' and ''after'' minimization in the vertical cross section along AA′ in Fig. 9d. Positive $\Delta Q_v (= Q_{v_{\text{after}}} - Q_{v_{\text{before}}})$ is shaded and ΔT $(= T_{\text{after}} - T_{\text{before}})$ is shown by solid line (warm anomaly) and dashed line (cold anomaly), respectively. Contour interval is 0.5°C. Differences in the wind field between ''before'' and ''after'' minimization are also shown as wind vectors.

initiation. Figure 13 shows vertical cross sections of moisture convergence and the vertical motion at the same location as in Fig. 12 at 0, 3, and 6 forecast hours. At the initial time of 2100 UTC, 4DVAR_SWD produces stronger moisture convergence than NO4DVAR below 1.4 km (~850 mb) as we can expect from Fig. 11 (see Figs. 13a,b). Comparing this with Fig. 12a, we note that the maximum moisture convergence is located right below the dry tongue southeast to the leading edge of the lid (marked by the contour of 316 K) with ascending motions. At 0000 UTC, NO4DVAR begins to produce noticeable moisture convergence near the surface and upward vertical motion over the region, but the intensity is still weaker than 4DVAR_SWD and its location lags behind that in 4DVAR_SWD (Figs. 13c,d). At 0300 UTC, the moisture convergence and rising motion in 4DVAR_SWD is westward tilted and is accompanied by strong compensating downward motion on the left side, which represents the complicated structure of the developing squall line (Fig. 13e). In NO4DVAR, moisture convergence is still very weak and distributed widely over a 100-km horizontal range in the boundary layer (Fig. 13f). The weak upward motion in association with the weak intensity of the surface cold front results in the weak and slow development of the squall line in NO4DVAR (cf. Figs. 13f and 13e). All these changes in 4DVAR_SWD lead to the improved forecast of precipitation in the squall line area, which will be shown later.

2) COMPARISON WITH PW ASSIMILATION

As explained in section 2, GPS-estimated precipitable water is simply the average of all available slant wet delays mapped to zenith over a 30-min time period. Since the individual phase delay can be accurately measured, it would be interesting to see what additional information can be obtained through the assimilation of slant wet delay, as compared to the assimilation of precipitable water through 4DVAR experiments. First, we examine the impact of SWD versus PW on the recovery of water vapor information. Figure 14 illustrates the differences in precipitable water between 4DVAR_SWD and 4DVAR_PW. The 4DVAR_SWD experiment produces more moisture in the squall-line area compared to 4DVAR_PW both at the initial state (Fig. 14a) and in the beginning stage of the squall line (Fig. 14b). One interesting point is that noticeable differences in PW exist between the receiver sites, which implies that the assimilation of slant wet delay can better recover the moisture information between the GPS receivers. Although a diagonal background error covariance matrix is used in our experiments, the attributes of the SWD observation operator help to spread the observed moisture information to grid points surrounding the receiver much more effectively in 4DVAR_SWD than in 4DVAR_PW.

Then, does the increased water vapor content derived from 4DVAR_SWD produce a positive impact on the prediction of atmospheric structure and the precipitation associated with the squall line? Figure 15 shows soundings from four experiments at the center of the squall line area at 0100 UTC, when the squall line begins to form. The Perfect_IC run shows low-level saturation and convective instability at this time, but the sounding in NO4DVAR is much drier and more stable. The 4DVAR_PW experiment shows saturation only near the surface. Moreover, the capping lid around 750 hPa still inhibits the updraft (Fig. 15d). With the assimilation of slant wet delay, the air from the surface to 750 hPa is completely saturated, which matches well with the low-level structure of the Perfect_IC run (cf. Figs. 15c and 15a). This indicates that 4DVAR_SWD performs better than 4DVAR_PW in the recovery of atmosphere thermodynamic structure in the squall-line area.

Next, to examine the impact of the SWD assimilation on the rainfall prediction, we compare the 3-hr accumulated rainfall ending at 0300 UTC from the four experiments (see Fig. 16). The heavy rainfall area extending from northeastern Kansas to southwestern Oklahoma, seen in the Perfect IC run, is not simulated in NO4DVAR. Instead, erroneous precipitation is generated over the northwestern Texas region (Fig. 16b). The 4DVAR_PW captures the rainfall area over Oklahoma fairly well, though with weaker intensity (Fig. 16d). With the assimilation of SWD, the forecast of the squall line and its associated heavy precipitation is much improved, especially over southern Kansas (Fig. 16c).

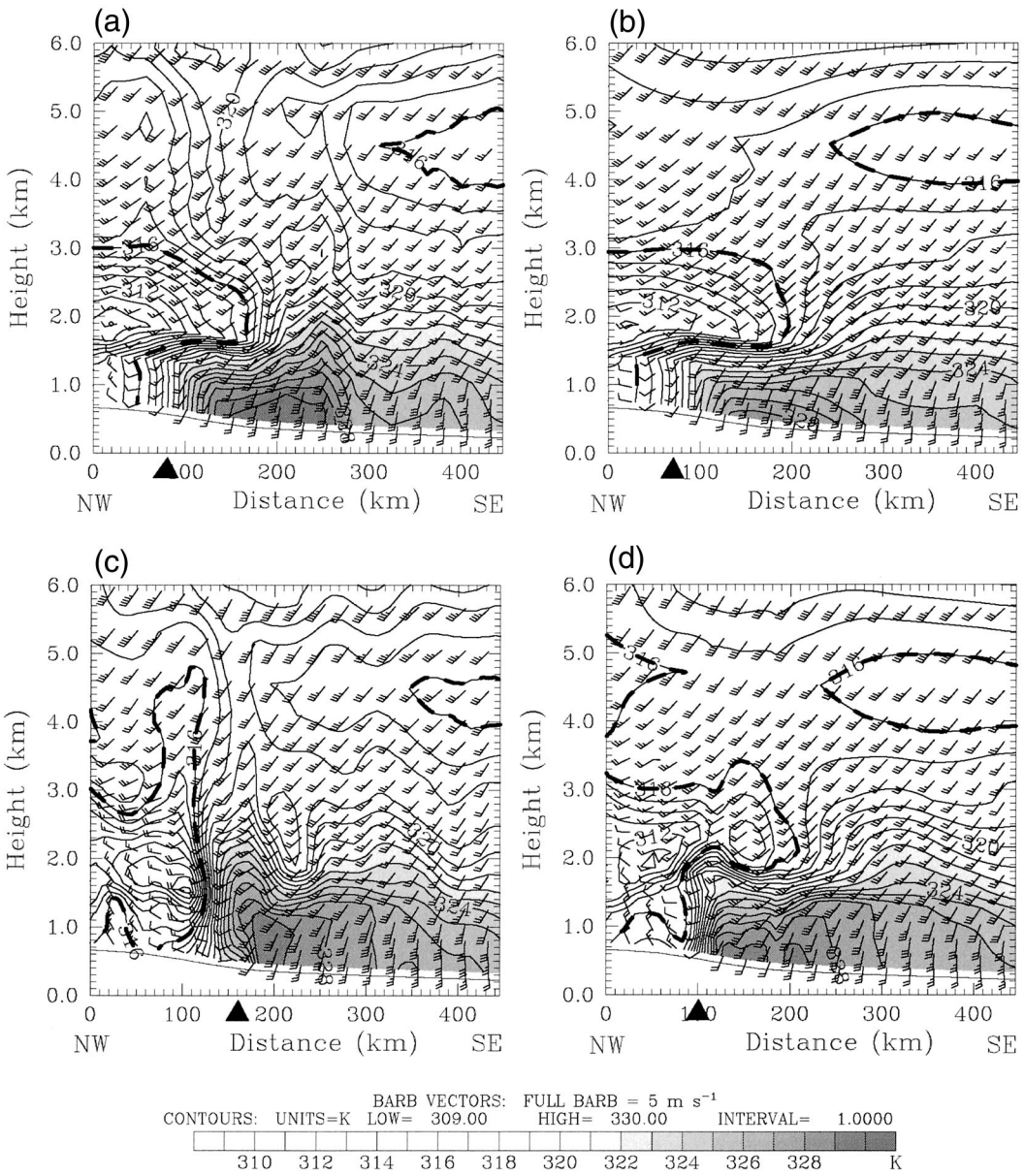

FIG. 12. Equivalent potential temperature and horizontal wind vectors along the solid line in Fig. 9d. (a), (c) 4DVAR_SWD and (b), (d) NO4DVAR at (a), (b) 0- and (c), (d) 3-h forecast time from the initial state at 2100 UTC 29 Oct. Full wind barb is 5 m s^{-1} and the thick dashed line is the contour of 316 K. The area greater than 320 K is shaded; ▲ indicates the location of the surface cold front.

Next, we examine the impact of SWD assimilation on the quantitative precipitation forecast (QPF). We confine the verification area to the squall-line region marked by a box in Fig. 16a. We calculate the threat score for the 4DVAR_SWD, 4DVAR_PW, and NO4DVAR experiments as verified against the Perfect_IC run. The results for the precipitation thresholds of 1, 5, 10, and 15 mm are presented in Fig. 17. Note that at 0000 UTC 30 October the squall line has not yet organized; while the forecast time of 0300 UTC corresponds to the initial stage, and 0600 UTC represents the developing stage of the squall line over the Kansas–Oklahoma region in Perfect_IC run. The large differences between 4DVAR experiments (4DVAR_PW and 4DVAR_SWD) and NO4DVAR in threat scores at the 1-mm threshold imply that the assimilation of GPS water vapor measurements can significantly improve the short-range prediction of precipitation (both in terms of location and intensity). Moreover, this improvement in QPF persists as the squall line evolves. It is important to note that 4DVAR_SWD has higher threat scores than 4DVAR_PW across all thresholds at all times.

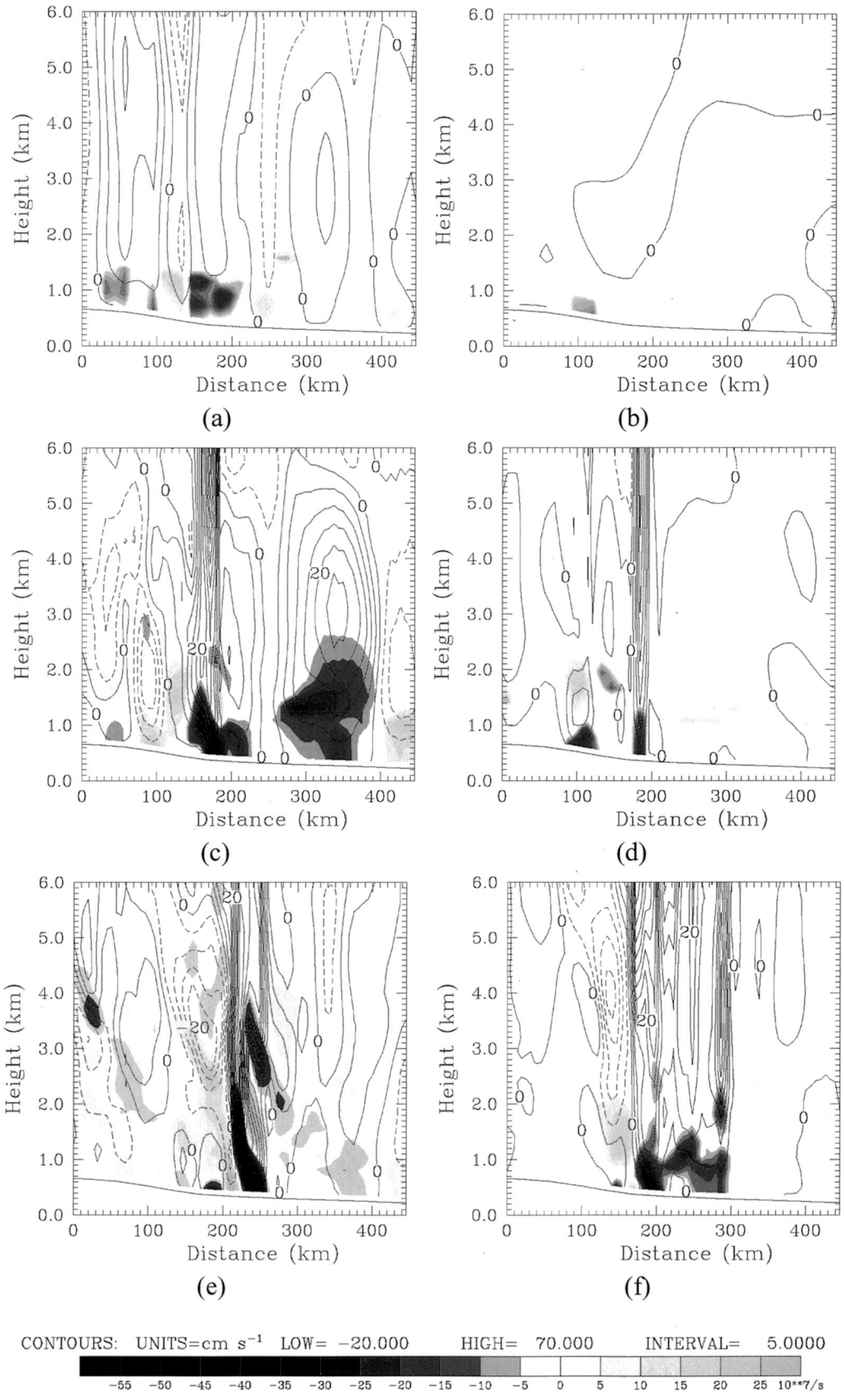
Height (km)
Distance (km)
(a)
(b)
(c)
(d)
(e)
(f)
CONTOURS: UNITS=cm s^{-1} LOW= −20.000 HIGH= 70.000 INTERVAL= 5.0000
−55 −50 −45 −40 −35 −30 −25 −20 −15 −10 −5 0 5 10 15 20 25 10**7/s

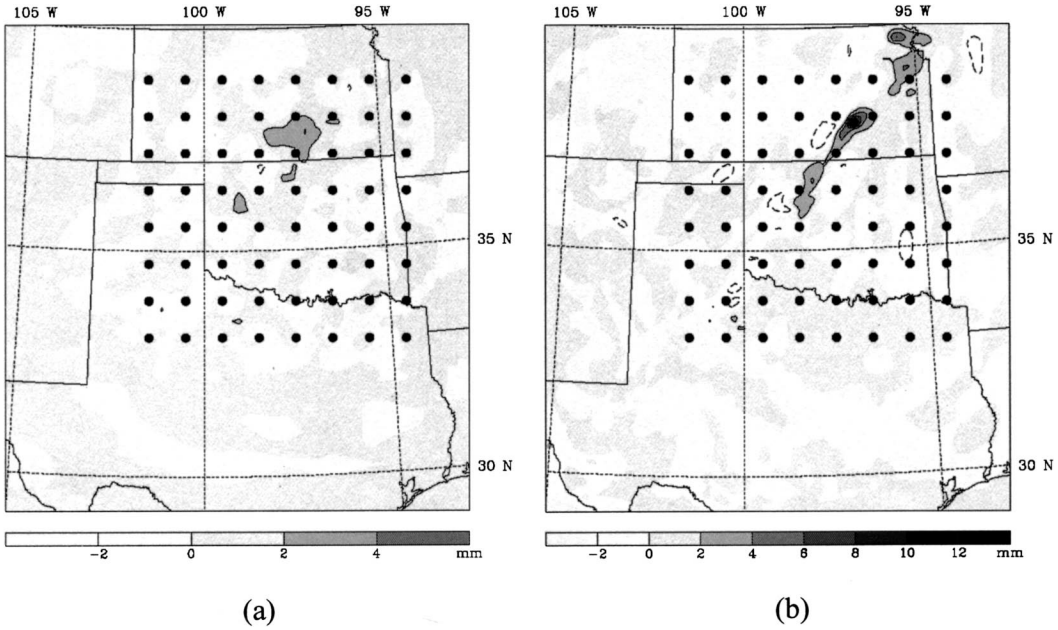

FIG. 14. Differences between 4DVAR_SWD and 4DVAR_PW at (a) 0-h forecast time valid at 2100 UTC 29 Oct and (b) 5-h forecast time valid at 0200 UTC 30 Oct. The value ΔPW ($=PW_{4DVAR\_SWD} - PW_{4DVAR\_PW}$) is positive for the solid line, negative for the dashed line. The shaded area represents positive ΔPW and the area greater than 2 mm is contoured with the interval of 2 mm. Dots indicate loci of the hypothetical ground-based GPS receiver sites.

4DVAR_PW significantly improves the prediction of the rainfall area (estimated by threat score at 1-mm threshold) over NO4DVAR, but fails to capture heavier rainfall, as shown by very low threat scores from the 5-mm threshold. As the SWD assimilation better recovers the detailed moisture structure in the squall-line area, 4DVAR_SWD has a stronger positive impact on the rainfall prediction throughout all threshold values.

5. Summary and conclusions

In this study, we performed a set of observing system simulation experiments to assess the impact of assimilating GPS slant wet delays on the short-range prediction of a prefrontal squall line. We first conducted a 3-km nature run using the MM5 model with an explicit moisture scheme. The results from the nature run were then used to simulate slant wet delay observations from a hypothetical network of 64 ground-based GPS receivers over the Oklahoma–Kansas region. These simulated slant wet delay data were, in turn, assimilated into a 27-km model using the MM5 4DVAR system with parameterized convection. Forward integration using a 9-km MM5 model, also with parameterized convection, was conducted based on the optimal initial condition obtained from the 27-km MM5 4DVAR run. There are two features in our experiment design that are worth mentioning: (i) the model used in the 3-km nature run to generate the ''observations'' is different from the assimilation model and the forecast model in terms of the resolution and model physics, therefore, the identical-twin problem in OSSE was partly removed; (ii) the assimilation model is different from the forecast model in terms of resolution and physics. This is similar to an incremental four-dimensional variational data assimilation approach, which has been implemented in the operational centers.

The analysis of our results leads to the following conclusions:

1) Modeling slant wet delay with a straight-line integration of wet refractivity is found to be accurate and computationally efficient for ray paths with elevation angles above 5°.
2) The assimilation of slant wet delay observations is highly effective in reducing the slant wet delay errors of the first guess field. After the assimilation, both the negative bias and the rms errors of the slant wet delay in the first guess field are significantly reduced.
3) The assimilation of slant wet delay not only improves the moisture fields (with changes of 1–2 g kg^{-1}), but also produces sizeable changes in the temperature

←

FIG. 13. Moisture divergence (shading) and vertical velocity (solid line) along the solid line AA′ in Fig. 9d at (a), (b) 1-, (c), (d) 3-, and (e), (f) 6-h forecast time. (left) 4DVAR_SWD and (right) NO4DVAR. Contour interval is 5 cm s^{-1}.

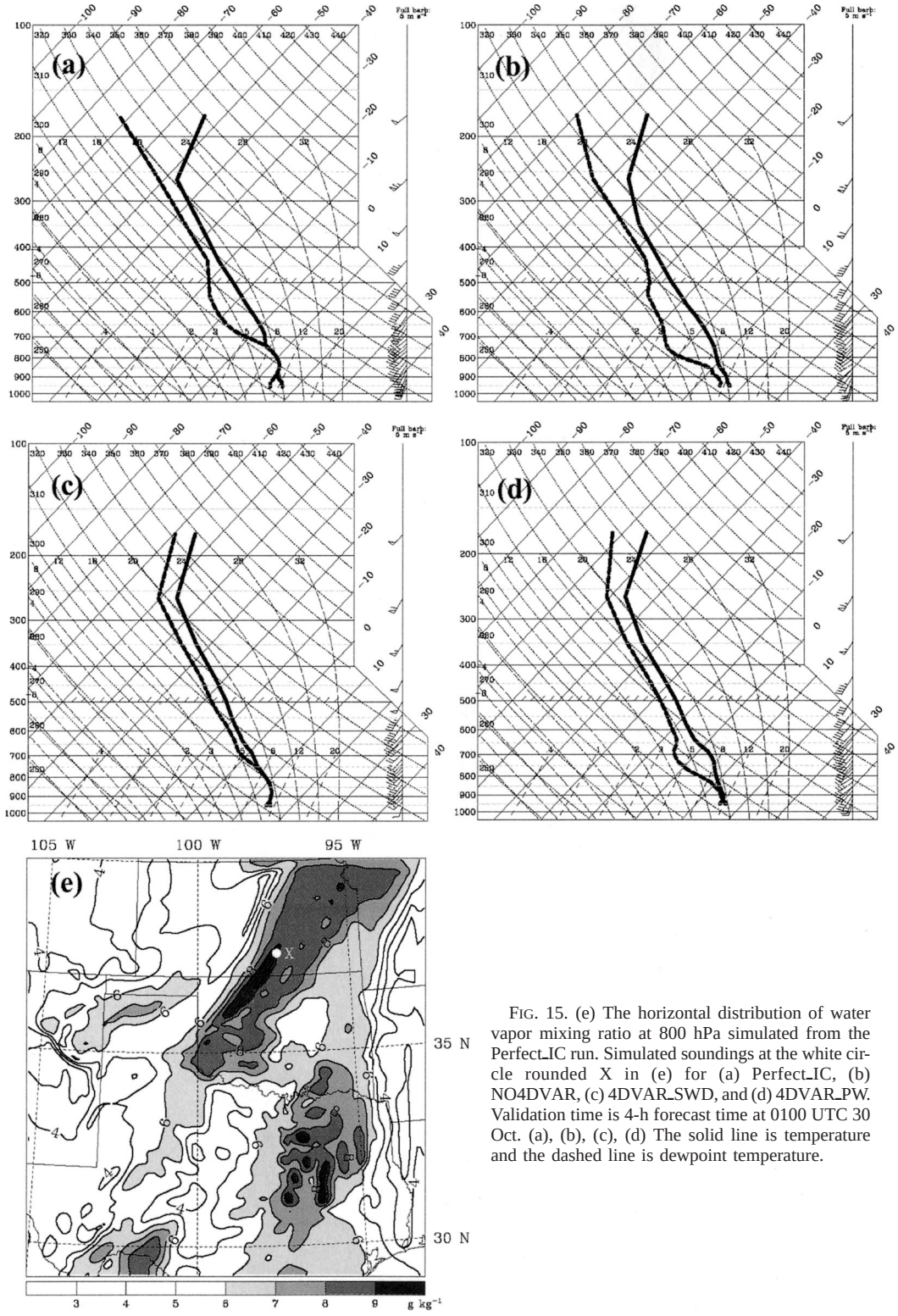

FIG. 15. (e) The horizontal distribution of water vapor mixing ratio at 800 hPa simulated from the Perfect_IC run. Simulated soundings at the white circle rounded X in (e) for (a) Perfect_IC, (b) NO4DVAR, (c) 4DVAR_SWD, and (d) 4DVAR_PW. Validation time is 4-h forecast time at 0100 UTC 30 Oct. (a), (b), (c), (d) The solid line is temperature and the dashed line is dewpoint temperature.

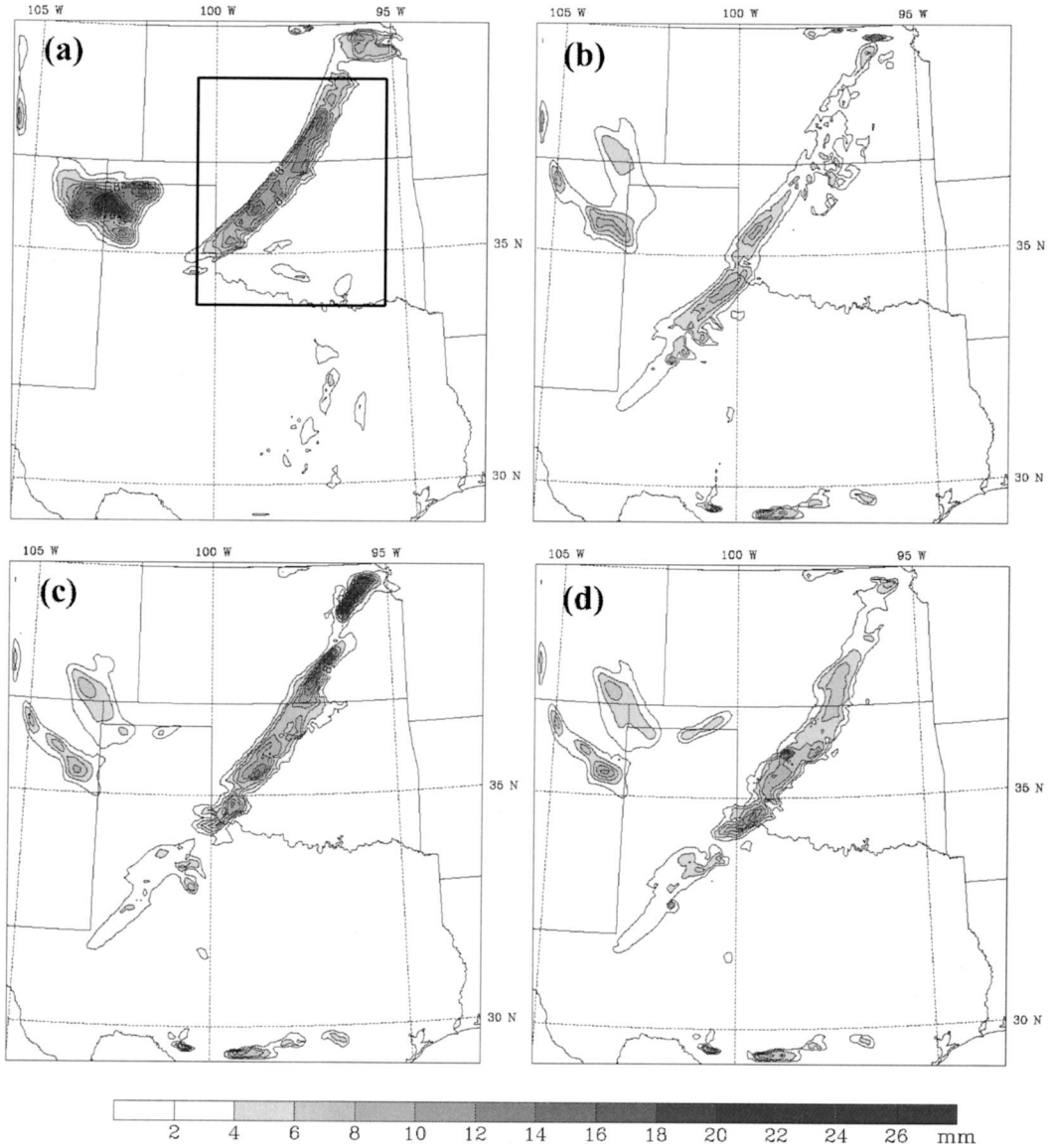

FIG. 16. The 3-h rainfall ending at 6-h forecast valid at 0300 UTC 30 Oct for (a) Perfect_IC, (b) NO4DVAR, (c) 4DVAR_SWD, and (d) 4DVAR_PW. Contour interval is 2 mm. (a) The box indicates the verification area for the calculation of threat scores in Fig. 17.

and wind fields in the lower troposphere, with a magnitude of 1°C and 3–5 m s^{-1}, respectively. Collectively, these changes produce warming and moistening ahead of the surface cold front. These changes are conducive to frontogenesis, and as a result a stronger surface cold front is produced. The enhanced surface cold front then supports a stronger transverse circulation and the low-level moisture convergence, allowing convection to be initiated with more accurate timing and intensity. As a result of slant wet delay assimilation, the squall line in the model develops at a time and location very close to the ''perfect'' initial condition run. This leads to accurate short-range quantitative precipitation forecast.

4) By comparing the results with precipitable water assimilation, we find that the assimilation of slant wet delay data is more effective in recovering moisture information, in particular, between the ground-based GPS stations. This is due to the fact that the slant wet delay data provide information on the spatial structure of moisture around the receiver site, while the precipitable water data provide moisture information only at the receiver site. The improved moisture recovery in slant wet delay assimilation produces a more accurate thermodynamic sounding, and a more accurate forecast of the squall-line evolution and its associated precipitation.

While the OSSE results presented in this paper are

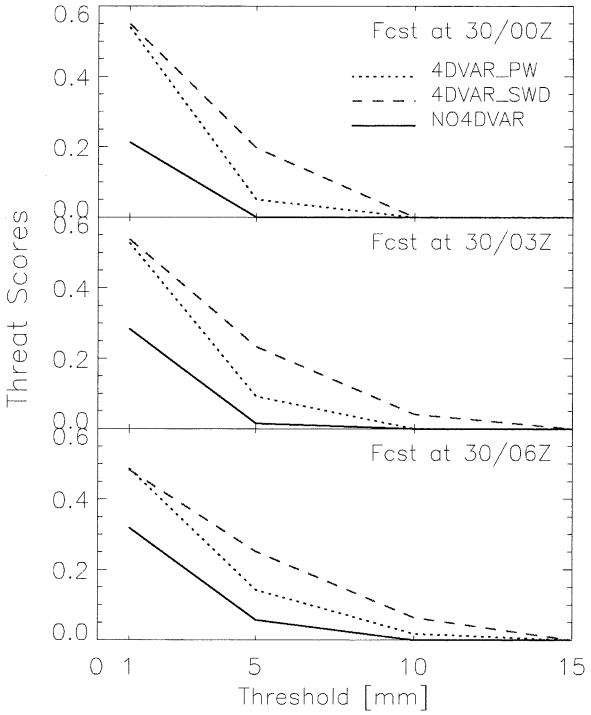

FIG. 17. Threat scores of 3-h accumulated rainfall from 4DVAR_SWD (dashed line), 4DVAR_PW (dotted line), and NO4DVAR (solid line) verified against the Perfect_IC run at 0000, 0300, and 0600 UTC 30 Oct.

encouraging and promising, one needs to recognize that assimilation of mesoscale observations (such as GPS slant wet delay data) in a convective environment is highly challenging. One major difficulty is the accuracy of the assimilation model. In this study, we are forced to use a 27-km MM5 for the assimilation of slant wet delay data, simply because of computational limitations. This requires the use of convective parameterization, which is, at best, a crude representation of ''observed'' convection as simulated by the explicit moisture scheme. In a real data assimilation study, the representation of convection in an assimilation model is likely to be an important source of errors. Ideally, one would like to use an assimilation model at cloud-resolving resolution and more accurate (or sophisticated) physics when advances in computational technology allow such an undertaking.

Despite the limitations of the assimilation model and the generally more optimistic results of the OSSE framework, the results presented in this paper give a clear indication that slant wet delay data from a ground-based GPS network is potentially highly valuable for short-range prediction of convective weather. A considerable amount of work is needed to improve the assimilation model, to estimate the relative benefits of 4DVAR to the three-dimensional variational (3DVAR) approach, to study the network design issues (e.g., spatial and temporal resolution of GPS receivers), and to test the assimilation system on real data cases. These problems will be addressed in subsequent papers.

Acknowledgments. The authors thank Dr. C. Rocken, Mr. J. Braun, and Ms. T. Van Hove for their helpful discussion about GPS data processing and their support. The encouragement and careful reviews of Drs. R. Ware, A. Crook, and J. Sun are also greatly appreciated. This research has been funded in part by DOE/ARM Grant DE-FG0302ER63327 and by the National Research Laboratory project Grant M1-0104-00-0006 of the Ministry of Science and Technology of South Korea. The first author acknowledges the financial support of NCAR Advanced Study Program and Brain Korea 21 program.

REFERENCES

Arnold, C. P., Jr., and C. H. Dey, 1986: Observing-systems simulation experiments: Past, present, and future. *Bull. Amer. Meteor. Soc.,* **67,** 687–694.

Bevis, M., S. Businger, S. Chiswell, T. Herring, R. Anthes, C. Rocken, and R. Ware, 1994: GPS meteorology: Mapping zenith wet delays onto precipitable water. *J. Appl. Meteor.,* **33,** 379–386.

Boudouris, G., 1963: On the index of refraction of the air, the absorption and dispersion of centimeter waves by gasses. *J. Res. Natl. Bur. Stand.,* **67,** 631–684.

Braun, J., C. Rocken, and R. Ware, 2001: Validation of line-of-sight water vapor measurements with GPS. *Radio Sci.,* **36,** 459–472.

Brooks, H. E., C. A. Doswell III, and L. J. Wicker, 1993: STORMTIPE: A forecasting experiment using a three-dimensional cloud model. *Wea. Forecasting,* **8,** 352–362.

Carlson, T. N., R. A. Anthes, M. Schwartz, S. G. Benjamin, and D. G. Baldwin, 1980: Analysis and prediction of severe storms environment. *Bull. Amer. Meteor. Soc.,* **61,** 1018–1032.

——, S. G. Benjamin, and G. S. Forbes, 1983: Elevated mixed layers in the regional severe storm environment: Conceptual model and case studies. *Mon. Wea. Rev.,* **111,** 1453–1473.

Crook, A. N., 1996: Sensitivity of moist convection forced by boundary layer processes to low-level thermodynamic fields. *Mon. Wea. Rev.,* **124,** 1767–1785.

Davis, J. L., T. A. Herring, I. I. Shapiro, A. E. E. Rogers, and G. Elgered, 1985: Geodesy by ratio interferometry: Effects of atmospheric modeling errors on estimates of baseline length. *Radio. Sci.,* **20,** 1593–1607.

——, G. Elgered, A. Niell, and C. Kuehn, 1993: Ground-based measurement of gradients in the ''wet'' radio refractivity of air. *Radio Sci.,* **29,** 1003–1018.

De Pondeca, M. S. F. V., and X. Zou, 2001a: Moisture retrievals from simulated zenith delay ''observations'' and their impact on short-range precipitation forecasts. *Tellus,* **53A,** 192–214.

——, and ——, 2001b: A case study of the variational assimilation of GPS zenith delay observations into a mesoscale model. *J. Appl. Meteor.,* **40,** 1559–1576.

Elosegui, P., A. Rius, J. Davis, G. Ruffini, S. Keihm, and B. Burki, 1998: An experiment for estimation of the spatial and temporal variations of water vapor using GPS and WVR data. *Phys. Chem. Earth,* **23,** 125–130.

Fankhauser, J. C., 1988: Estimates of thunderstorm precipitation efficiency from field measurements in CCOPE. *Mon. Wea. Rev.,* **116,** 663–684.

Grell, G. A., J. Dudhia, and D. R. Stauffer, 1994: A description of the fifth-generation Penn State/NCAR Mesoscale Model (MM5). Tech. Note TN-398+IA, National Center for Atmospheric Research, Boulder, CO, 125 pp.

Guo, Y.-R., and S. Chen, 1994: Terrain and land use for the fifth-generation Penn State/NCAR Mesoscale Modeling System

(MM5): Program TERRAIN. Tech. Note TN-397+1A, National Center for Atmospheric Research, Boulder, CO, 114 pp.
——, Y.-H. Kuo, J. Dudhia, D. Parsons, and C. Rocken, 2000: Four-dimensional variational data assimilation of heterogeneous mesoscale observations for a strong convective case. *Mon. Wea. Rev.*, **128,** 619–643.
Ha, S.-Y., Y.-H. Kuo, Y.-R. Guo, C. Rocken, and T. van Hove, 2002: Comparison of GPS slant wet delay measurements with model simulations during the passage of a squall line. *Geophys. Res. Lett.*, **29,** 2113, doi:10.1029/2002GL015891.
Hobbs, P. V., J. D. Locatelli, and J. E. Martin, 1990: Cold fronts aloft and the forecasting of precipitation and severe weather east of the Rocky Mountains. *Wea. Forecasting*, **5,** 613–626.
Hong, S.-Y., and H.-L. Pan, 1996: Nonlocal boundary layer vertical diffusion in a medium-range forecast model. *Mon. Wea. Rev.*, **124,** 2322–2339.
Kuo, Y.-H., Y.-R. Guo, and E. R. Westwater, 1993: Assimilation of precipitable water measurements into a mesoscale numerical model. *Mon. Wea. Rev.*, **121,** 1215–1238.
——, X. Zou, and Y.-R. Guo, 1996: Variational assimilation of precipitable water using a nonhydrostatic mesoscale adjoint model. Part I: Moisture retrieval and sensitivity experiments. *Mon. Wea. Rev.*, **124,** 122–147.
Lee, B. D., R. D. Farley, and M. R. Hjelmfelt, 1991: A numerical case study of convection initiation along colliding convergence boundaries in northeast Colorado. *J. Atmos. Sci.*, **48,** 2350–2366.
Locatelli, J. D., J. E. Martin, J. A. Castle, and P. V. Hobbs, 1995: Structure and evolution of winter cyclones in the central United States and their effects on the distribution of precipitation. Part III: The development of a squall line associated with weak cold frontogenesis aloft. *Mon. Wea. Rev.*, **123,** 2641–2662.
——, M. T. Stoelinga, and P. V. Hobbs, 1998: Structure and evolution of winter cyclones in the central United States and their effects on the distribution of precipitation. Part V: Thermodynamic and dual-Doppler radar analysis of a squall line associated with a cold front aloft. *Mon. Wea. Rev.*, **126,** 860–875.
MacDonald, A., Y. Xie, and R. Ware, 2002: Diagnosis of three-dimensional water vapor using a GPS network. *Mon. Wea. Rev.*, **130,** 386–397.
Martin, J. E., 1998: The structure and evolution of a continental winter cyclone. Part I: Frontal structure and the occlusion process. *Mon. Wea. Rev.*, **126,** 303–328.
——, J. D. Locatelli, P. V. Hobbs, P.-Y. Wang, and J. A. Castle, 1995: Structure and evolution of winter cyclones in the central United States and their effects on the distribution of precipitation. Part I: A synoptic-scale rainband associated with a dryline and a lee trough. *Mon. Wea. Rev.*, **123,** 241–264.
Navon, I. M., X. Zou, J. Derber, and J. Sela, 1992: Variational data assimilation with an adiabatic version of the NMC spectral model. *Mon. Wea. Rev.*, **120,** 1433–1446.
Niell, A. E., 1996: Global mapping functions for the atmosphere delay at radio wavelengths. *J. Geophys. Res.*, **101** (B2), 3227–3246.
Pany, T., 2002: Measuring and modeling the slant wet delay with GPS and the ECMWF NWP model. *Phys. Chem. Earth*, **27A,** 347–354.
——, P. Pesec, and G. Stangl, 2001: Atmospheric GPS slant path delays and ray-tracing through numerical weather models: A comparison. *Phys. Chem. Earth*, **26A,** 183–188.
Resch, G. M., 1984: Water vapor radiometry in geodetic applications. *Geodetic Refraction*, F. K. Brunner, Ed., Springer-Verlag, 53–84.
Rinehart, 1989: *Radar for Meteorologists.* University of North Dakota, 218 pp.
Rocken, C., T. van Hove, J. Johnson, F. Solheim, R. Ware, M. Bevis, S. Chiswell, and S. Businger, 1995: GPS/STORM—GPS sensing of atmospheric water vapor for meteorology. *J. Atmos. Oceanic Technol.*, **12,** 468–478.
Vandenberghe, F., and Y.-R. Guo, 2000: Improved tropospheric delay measurement and precision orbit determination for satellite ocean altimetry. JPL/NCAR Project Report, 17 pp.
Ware, R., C. Alber, C. Rocken, and F. Solheim, 1997: Sensing integrated water vapor along GPS ray paths. *Geophys. Res. Lett.*, **24,** 417–420.
——, and Coauthors, 2000: SuomiNet: A real-time national GPS network for atmospheric research and education. *Bull. Amer. Meteor. Soc.*, **81,** 677–694.
Watson, A. I., and D. O. Blanchard, 1984: The relationship between the total area divergence and convective precipitation in south Florida. *Mon. Wea. Rev.*, **112,** 673–685.
Zou, X., F. Vandenberghe, M. Pondeca, and Y.-H. Kuo, 1997: Introduction to adjoint techniques and the MM5 adjoint modeling system. NCAR Tech. Note NCAR/TN-435-STR, National Center for Atmospheric Research, Boulder, CO, 110 pp.
——, and Coauthors, 1999: A ray-tracing operator and its adjoint for the use of GPS/MET refraction angle measurements. *J. Geophys. Res.*, **104** (D18), 22 301–22 318.